

Superconductivity at 48 K of heavily hydrogen-doped SmFeAsO epitaxial films grown by topotactic chemical reaction using CaH₂

Jumpei Matsumoto (1), Kota Hanzawa (1), Masato Sasase (2), Silvia Haindl (3),
Takayoshi Katase (1), Hidenori Hiramatsu (1,2,a), and Hideo Hosono (1,2)

(1) Laboratory for Materials and Structures, Institute of Innovative Research, Tokyo Institute of Technology, Mailbox R3-3, 4259 Nagatsuta-cho, Midori-ku, Yokohama, Kanagawa 226-8503, Japan

(2) Materials Research Center for Element Strategy, Tokyo Institute of Technology, Mailbox SE-1, 4259 Nagatsuta-cho, Midori-ku, Yokohama, Kanagawa 226-8503, Japan

(3) World Research Hub Initiative (WRHI), Institute of Innovative Research, Tokyo Institute of Technology, 4259 Nagatsuta-cho, Midori-ku, Yokohama, Kanagawa 226-8503, Japan

Abstract

High critical-temperature (T_c) superconductivity at 48 K is reported for hydrogen-doped SmFeAsO epitaxial films on MgO single-crystal substrates. The key processes are pulsed laser deposition to grow undoped SmFeAsO epitaxial films and subsequent topotactic chemical reaction using CaH₂ powders under evacuated silica-glass ampule atmosphere. This post-deposition thermal annealing treatment we have developed realizes maximum hydrogen concentration $x = \sim 0.35$ in SmFeAs(O_{1-x}H_x). Disordered hydrogen-substitution at O sites is experimentally confirmed directly by atomic-scale microstructure observation. Complete diamagnetism in magnetization measurements validates the bulk nature of the high- T_c superconductivity in the films. This method will become an effective and general method to fabricate various high-quality oxyhydride epitaxial films.

a) Electronic mail: h-hirama@mces.titech.ac.jp

In 2008, Kamihara *et al.* reported that ca. 10%-F-doping at O site of LaFeAsO induces superconductivity at critical temperature (T_c) = 26 K [1], which was 2 years later from their report on superconductivity at T_c = 4 K of LaFePO [2]. Both of them crystallize in the ZrCuSiAs-type structure and are called 1111-type Fe-based superconductors. They are isomorphic to wide-gap p-type layered oxychalcogenide semiconductors ReCuOCh (Re = rare earth, Ch = chalcogen) [3, 4]. Usually, Fe with its large magnetic moment is believed to be harmful to the emergence of superconductivity and similar assumptions were also applied to other magnetic 3d transition metals such as Ni and Co. Thus, the above discovery of high- T_c superconductivity at 26 K in F-doped LaFeAsO [1] was accepted with surprise in the condensed matter community and globally rekindled extensive exploration studies of new superconductors [5]. These materials have since grown to be a new class of high- T_c superconductors and they have characteristic features for future practical applications such as superconductor wires, tapes, and coated conductors for high-field magnets [6–9].

The maximum T_c among the Fe-based superconductors is ca. 55 K, which is reported for F-doped 1111-type SmFeAsO [10], called Sm1111. The substitution limit of fluorine is ~20% with respect to its O site. However, Hanna *et al.* [11] reported that oxygen can also be replaced by hydrogen with the maximum T_c in H-doped Sm1111 [$\text{SmFeAs(O}_{1-x}\text{H}_x\text{)}$] comparable to that of F-doped Sm1111. The most important characteristics of H doping is that the substitution limit extends to ~80% (i.e. x = 0.8), leading to the discovery of unique electronic phase diagrams of 1111-type ReFeAsO [11–13]. It is considered that in both cases, H-doped as well as F-doped SmFeAsO, superconductivity originates from electron doping by substitution at the O site. Although small size crystals with max. ~400 μm were reported recently [14], it is very difficult to grow

enough large-size single crystals of H-doped Sm1111, which restricts more detailed investigations on the superconducting mechanism and the electronic band structure by experimental methods such like angle-resolved photoemission spectroscopy.

We therefore propose another synthesis approach in order to make future studies on H-doped Sm1111 accessible. Here, we report on large size heteroepitaxial thin-film samples on single-crystalline substrates with a usual lateral size of 10mm × 10mm. Just after the report by Kamihara *et al.* in 2008 [1], extensive synthesis and research did not only start on bulk samples (polycrystalline and single crystals) but also thin film growth – especially epitaxial films – was stimulated world wide [8, 9, 15, 16]. Pulsed laser deposition (PLD) turned out to be the most compatible technique also for Fe-based superconductors and has been employed mainly because of the historical success in the growth of high- T_c cuprate thin films and coated conductors. It is important to note here that until today epitaxial ReFeAsO thin films could not been grown by PLD equipped with an ultraviolet KrF excimer laser ($\lambda = 248$ nm). A KrF laser in a room-temperature deposition was employed only for chemical transfer before a post-deposition thermal annealing of La1111 films [17, 18]. Hiramatsu *et al.* [19] thus employed a Nd:YAG laser, instead of an ultraviolet excimer laser as an excitation for the PLD process, initially demonstrating in-situ La1111 heteroepitaxial growth. Utilizing this Nd:YAG PLD system, Haindl *et al.* [20–23] recently realized in-situ PLD growth of high-quality undoped and F-doped Sm1111 epitaxial films. At present, besides PLD, molecular beam epitaxy (MBE) is a common technique for the in-situ growth of 1111-type ReFeAsO films [24, 25], and metal-organic chemical vapor deposition has made progress in the fabrication of 1111-type ReFeAsO films [26]. Our studies on in-situ PLD growth of ReFeAsO imply that the optimization of growth conditions is severe irrespective of use

of a Nd:YAG laser for ablation [21, 22] and any attempts to achieve in-situ PLD growth of H-doped Sm1111 epitaxial films failed so far. Even our initial efforts in a reactive PLD process demonstrated that hydrogen could not be doped into epitaxial Sm1111 films when H₂ gas and rf-generated H radical gas were introduced into the growth chamber during deposition experiments, which will be discussed later in Fig. S1. The essential key in this study is a topotactic chemical reaction between undoped Sm1111 epitaxial films, grown by the Nd:YAG PLD, and CaH₂ powder using a unique post-deposition thermal annealing experimental setup. We successfully demonstrate the high- T_c bulk superconductivity at 48 K of H-doped Sm1111 epitaxial films on MgO single-crystalline substrates and would lead to future experimental validation of mechanism of high- T_c superconductivity of 1111-type Fe-based superconductors.

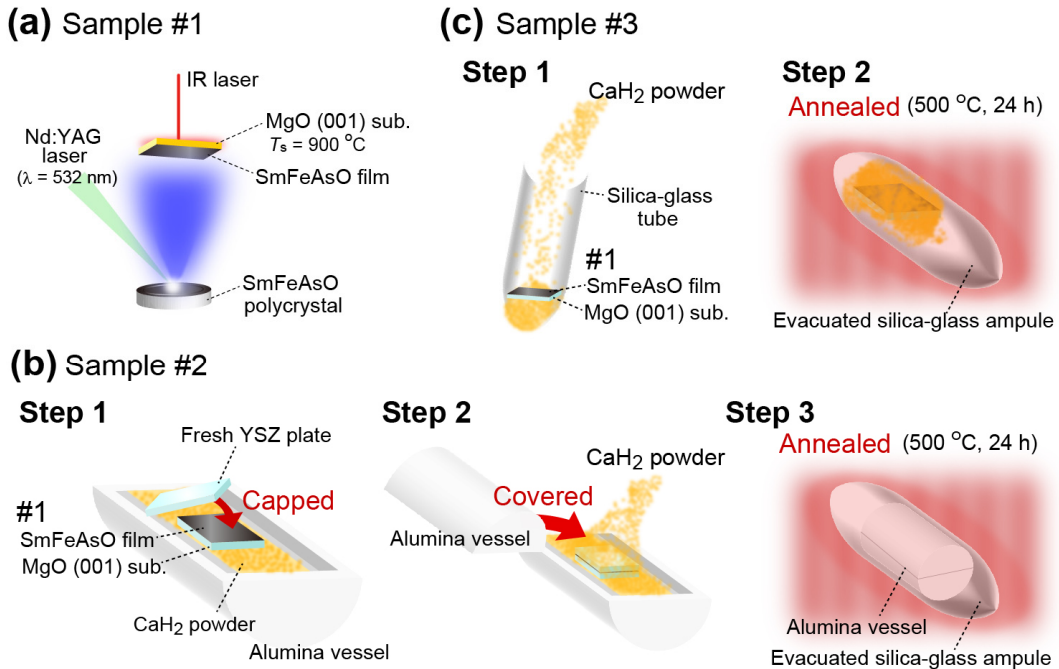


Figure 1. Fabrication procedure of H-doped SmFeAsO (Sm1111) epitaxial thin films.

(a) A schematic image for growth of an undoped Sm1111 epitaxial precursor film (#1) by Nd:YAG PLD under high vacuum. (b) H-doping of the Sm1111 epitaxial precursor film. In step 1, the precursor (#1) was capped by a YSZ single-crystalline plate and put into an alumina vessel filled with CaH₂ powder. In step 2 the alumina vessel is closed. In step 3 the vessel was subsequently sealed in a silica-glass ampule and thermally annealed in vacuum at 500°C for 24h. The resulting H-doped Sm1111 film is denoted as #2. (c) Heavily H-doped Sm1111 epitaxial thin film: In step 1, the precursor film was inserted into a silica-glass tube that was filled with CaH₂ powder. In step 2 the tube was sealed under vacuum and then thermally annealed at 500 °C for 24h. The heavily H-doped Sm1111 film is denoted as #3.

Sample fabrication and characterization

Figure 1a shows growth process of undoped Sm1111 heteroepitaxial thin films. PLD using second harmonics ($\lambda = 532$ nm) of a Nd:YAG laser ablated undoped Sm1111 polycrystalline disks and deposited the films on MgO single-crystalline substrates (size: 10mm \times 10mm \times 0.5mm), heated at 900°C with an infrared semiconductor laser, under a high vacuum atmosphere (base pressure: $\sim 1 \times 10^{-6}$ Pa). The MgO substrate was thermally annealed at 1050 °C in air before deposition. The thicknesses of all the undoped Sm1111 films were fixed to be ~ 80 nm. The Nd:YAG PLD-film-growth procedure was carried out according to the details reported in refs. [19–22]. These undoped Sm1111 epitaxial films grown by the Nd:YAG PLD are called precursor films (#1) and serve as starting point in this study. Although we initially attempted H-doping of Sm1111 epitaxial films by in-situ growth under H₂ gas and rf-generated H radical atmospheres as well as by post-deposition thermal annealing treatment under H₂ atmosphere, no H-doped Sm1111 films could be obtained. To efficiently dope H into the Sm1111 epitaxial films, we therefore performed a topotactic chemical reaction using an active solid H-source, which is CaH₂ polycrystalline powder, through two different experimental approaches (Figs. 1 b,c). The topotactic chemical reaction we expected for both was $\text{SmFeAsO} + (x/2)\text{CaH}_2 \rightarrow \text{SmFeAs(O}_{1-x}\text{H}_x\text{)} + (x/2)\text{CaO}$. Figure 1b represents the first approach, which is based on our previous reports on heteroepitaxial growth of materials composed of high vapor pressure elements such as K [27, 28]. The precursor film (#1) was put at the bottom of an alumina vessel, which was preliminary paved by large amounts of CaH₂ powder to keep high H vapor pressure during subsequent thermal annealing process, and then capped with a Y-stabilized ZrO₂ (YSZ) single-crystal plate to protect surface of the undoped Sm1111 film. More CaH₂ powder

was put on the YSZ plate, and then sealed with an alumina top cover. Finally, the alumina vessel was thermally annealed in an evacuated silica-glass ampule at 500 °C for 24 h. The resulting H-doped film is defined as sample #2. The second approach resulted in heavy H-doped films (#3) that were fabricated through two steps similar with #2 as shown in Fig 1c. Here, the precursor film (#1) was directly filled together with large amounts of CaH₂ powder in silica-glass tube and subsequently sealed under a vacuum atmosphere in silica-glass ampule, i.e., this approach does not employ a film surface protection with YSZ and efficiently promotes the topotactic reaction and diffusion of hydrogen into the film. The final thermal annealing process condition is carried out under the same conditions as that for #2.

The crystalline phases and structure parameters such as lattice parameters were characterized by X-ray diffraction (XRD) with monochromated Cu K α_1 radiation. The crystallinity and crystallographic orientation of resulting Sm1111 films were evaluated by X-ray rocking-curve measurements at the Sm1111 003 diffraction for the out-of-plane direction and at the Sm1111 200 diffraction for the in-plane direction. Scanning transmission electron microscope (STEM) with high-angle annular dark field (HAADF) and annular bright-field (ABF) modes was employed for the observation of atomic-scale cross-sectional microstructure. H concentration [x in SmFeAs(O_{1-x}H_x)] of the H-doped Sm1111 epitaxial films was quantitatively determined from depth profiles obtained by secondary ion mass spectroscopy (SIMS) using a polycrystalline SmFeAs(O_{0.4}H_{0.6}) bulk sample [13] as a standard sample. Temperature (T) dependence of the electrical resistivity (ρ) was measured using four-probe method with Au electrodes from 2 K to 300 K under magnetic fields up to 9 T. Magnetization was characterized at $T = 4\text{--}300$ K using zero-field cooling (ZFC) and field cooling (FC) at

10 Oe to confirm the bulk superconductivity in the H-doped Sm1111 films #2 and #3 (i.e., complete diamagnetism).

Thin-film growth by Nd:YAG PLD and thermal annealing

Before we employed the topotactic chemical reaction using CaH₂ powder as an active H-source for H doping, we preliminarily attempted H doping during reactive in-situ PLD film-growth as well as by post-deposition thermal annealing under H₂ atmosphere. Figure S1 summarizes the resultant XRD patterns and $\rho-T$ curves in each employed process. Figures S1a and S1c display H pressure (P_{H_2}) dependence of obtained crystalline phases, where H₂ gas and rf-generated H radical gas were introduced into the vacuum chamber for PLD growth during the film growth experiments, respectively. In both processes, impurity phases such as SmAs segregated with the increase in P_{H_2} . Furthermore, their $\rho-T$ behavior maintained insulator-like [19, 20, 29 – 31] as shown in Figs. S1b for H₂-gas growth and S1d for growth with the rf-H radical source. Then, we performed post-deposition thermal annealing under H₂ gas atmosphere for as-grown Sm1111 epitaxial thin films, which were deposited under a high vacuum at 800 °C. Figures S1e and S1f are XRD patterns and $\rho-T$ curves before and after the annealing, respectively. Similar to both above attempts of a reactive in-situ growth, this post-deposition annealing process could not induce a superconducting transition either. These results suggested that hydrogen was not substituted for oxygen probably due to the strong chemical bonding between O and Sm within the O-Sm layers of the layered crystal structure.

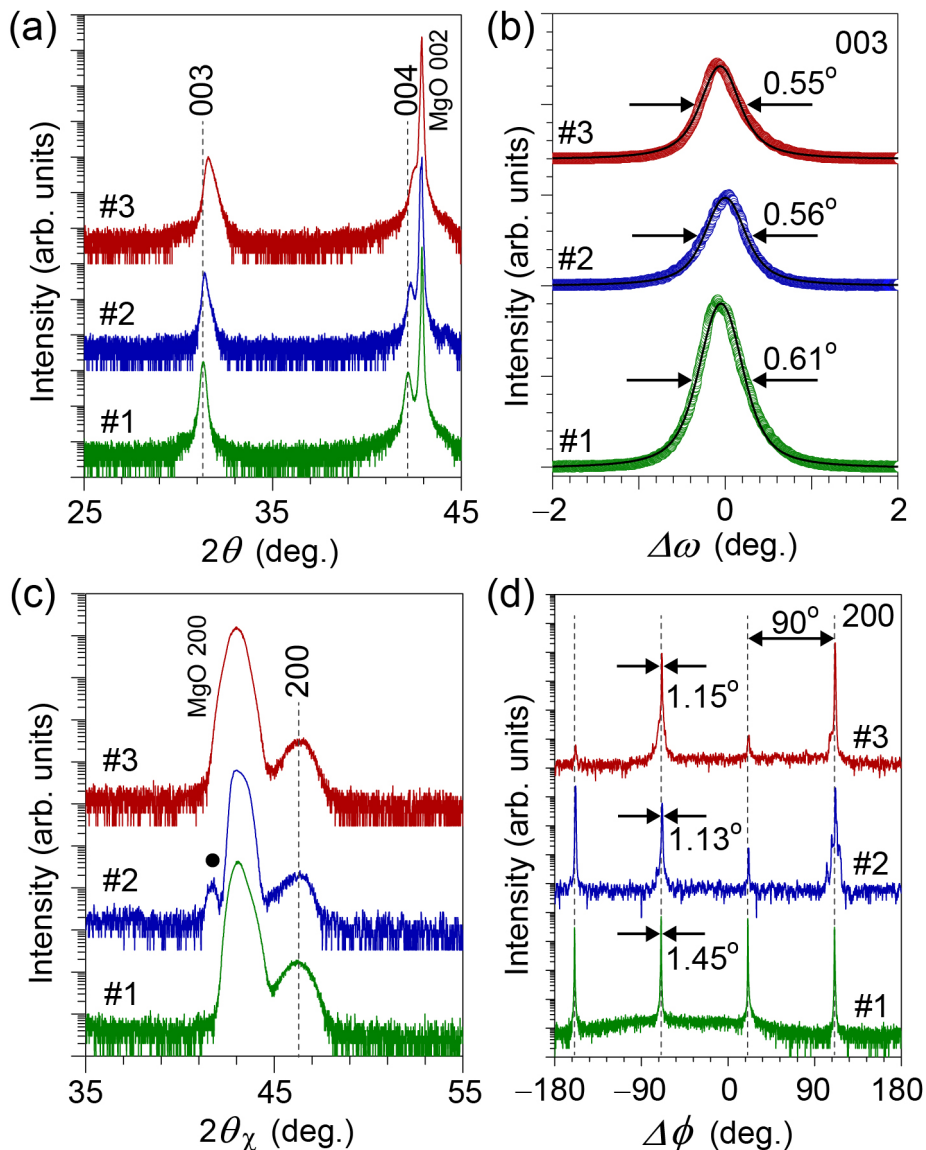


Figure 2. Structural analyses of the undoped precursor film (#1) and H-doped Sm1111 epitaxial thin films (#2, 3). (a) out-of-plane XRD patterns (b) 003 rocking curves of samples #1, #2, and #3. (c) in-plane XRD patterns of samples #1, #2, and #3. Filled circle in (c) represents a diffraction of an impurity phase such as As_2O_5 . (d) In-plane symmetry of Sm1111 200 diffractions.

Topotactic chemical reaction using CaH_2

Thus, we performed a post-deposition thermal annealing on undoped precursor films

using the binary hydride CaH_2 as a more active solid H-source in order to achieve high partial pressures (i.e., chemical potential) of hydrogen during the chemical reaction that finally result in hydrogen substitution for oxygen of undoped Sm1111 epitaxial films preliminarily grown by PLD. Figure 2a shows out-of-plane XRD patterns of three Sm1111 films (wider 2θ range patterns are shown in Fig. S2a). Undoped Sm1111, #1, exhibited strong *c*-axis orientation without any impurity phases for out-of-plane. This feature did not change in thermally annealed samples of #2 and #3. Figure 2b displays out-of-plane rocking curves of the 003 diffraction. The full widths at half maxima are all $\sim 0.6^\circ$. Figures 2c and 2d show the in-plane XRD patterns (wider $2\theta\chi$ range patterns are shown in Fig. S2b) and in-plane rocking curves, respectively. For #1 and #3, only diffractions of the Sm1111 phase and the MgO substrate were observed (Fig. 2c), whereas for #2, an impurity phase indicated by a filled circle, was detected, whose possible candidate was 400 diffraction of As_2O_5 . Because from the in-plane four-fold symmetry reflecting the tetragonal lattice of Sm1111 observed in Fig 2d, we concluded that the Sm1111 lattice maintained a heteroepitaxial relation with the MgO substrate, $[001]\text{SmFeAsO} \parallel [001]\text{MgO}$ for out-of-plane and $[100]\text{ SmFeAsO} \parallel [100]\text{ MgO}$ for in-plane, which remains unchanged under additional thermal annealing and the topotactic chemical reaction. From these XRD patterns, we estimated the *a*- and *c*-axes lattice parameters. For the undoped precursor film (#1), we would like to note that an *a*-axis lattice parameter of 3.923 \AA irrespective of the larger in-plane lattice parameter of MgO substrate ($a = 4.213\text{ \AA}$), and a *c*-axes lattice parameter of 8.561 \AA , clearly different to the lattice parameters of undoped polycrystalline bulk ($a = 3.9395$ and $c = 8.4969\text{ \AA}$ [11]). This would originate from lattice strain due to heteroepitaxial growth. In the case of H-doping of Sm1111 polycrystalline bulks, the lattice parameters

continuously decrease both along a - and c -axes with increasing H concentration x [11]. Accordingly, the lattice parameters of our epitaxial films also shrank in the order from #1, #2 ($a = 3.912$ and $c = 8.534$ Å), to #3 ($a = 3.903$ and $c = 8.488$ Å). This implies indirectly that an increasing amount of H is incorporated into the Sm1111 epitaxial films in this sample numbering order.

Atomic-scale microstructure observation

We then observed atomic-scale microstructure of the sample #3, in which the highest H concentration was expected based on the above lattice parameters' analysis. Figure 3a shows wide-view cross-sectional microstructure. Originating from its layered crystal structure, alternately stacking patterns along the c -axis were clearly observed from interface to film surface without any defects such as dislocations in this scale, validating its high film-quality. The interface shown in the inset was very sharp (i.e., heteroepitaxial growth starts from a few atomic layers.), indicating that any chemical reaction between the film and the MgO does not occur during the in-situ PLD growth and the post-deposition thermal annealing. The atomic resolution HAADF-STEM image (Fig. 3b) indicates that the observed image is atomically consistent with the 1111-type layered structure. But we could not observe clear Z-contrast originating from H substitution at O site in this image because the contrast of neighbor Sm, which bonds with O, was too bright with respect to O signals. It should be noted that in Fig. 3c we attained clear experimental evidence for hydrogen substitution at O site by ABF-STEM. In this figure, originating from its bright-field characteristics, the darkest and largest ones are Sm positions, and some O atoms at O sites are indicated by yellow arrows. We found that brighter positions indicated by light blue arrows also exist at the same O sites.

This observation result is the clear experimental evidence that doped H substitutes at the O site and it is completely disordered. This substitution is also confirmed in the intensity plot at the bottom of Fig. 3(c).

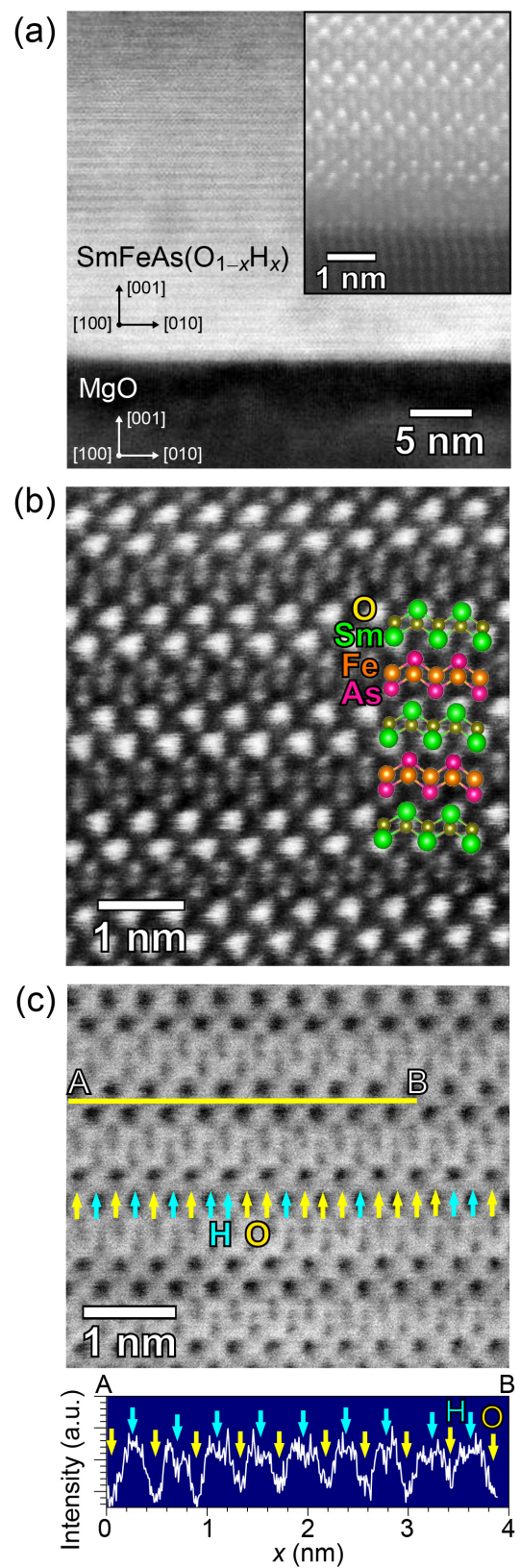


Figure 3. Cross-sectional microstructure analysis of the sample #3. The incident

electron beam was along the a -axis of Sm1111. (a) Wide-view HAADF-STEM image. The inset shows atomic resolution interface between the film and MgO. (b) The atomic-resolution HAADF-STEM image in the Sm1111 film region. (c) atomic-resolution ABF-STEM image in the Sm1111 film region. O and H atoms at O sites are indicated by yellow and light blue arrows, respectively. The bottom panel is the intensity plot along the line A – B in the upper ABF-STEM image.

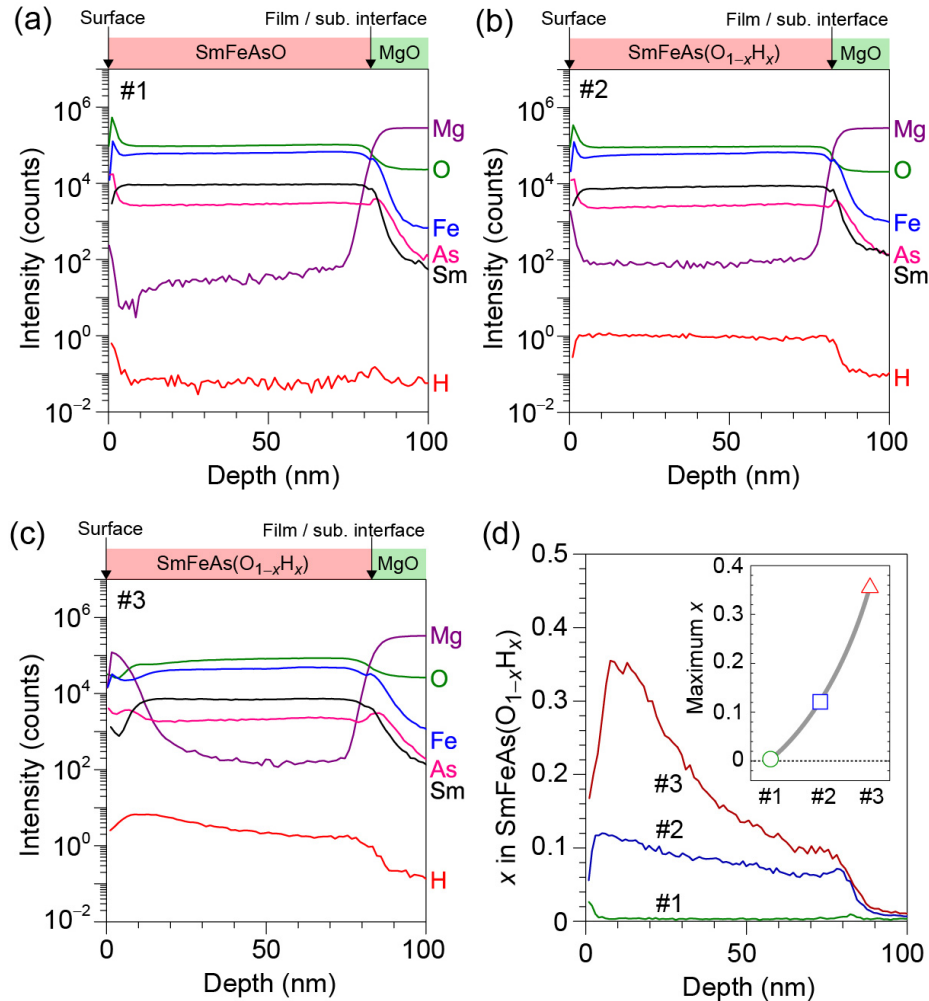


Figure 4. H concentration (x) in $\text{SmFeAs}(\text{O}_{1-x}\text{H}_x)$ epitaxial thin films. SIMS profiles of (a) #1, (b) #2, and (c) #3 as a function of depth from surface, i.e., depth of 0 nm denotes

the top of the film surface. These profiles were normalized with respect to the Fe signal.

(d) Depth dependence of x for all three films (#1, #2, #3). The inset shows the maximum x for each sample.

H concentration in the films

According to the above long-range (i.e., entirely averaged in XRD) and local atomic-scale structural analyses by STEM, H-doping of Sm1111 epitaxial films was successfully introduced by the CaH₂ route. Hence, we then quantitatively analyzed H concentrations [x in SmFeAs(O_{1-x}H_x)] in all the samples by SIMS. Figures 4a–4c show SIMS depth profiles for samples #1, #2, and #3, respectively. Figure 4d is a summary of these profiles in terms of hydrogen signal. Although the H signal for #1 was almost comparable to the detection limit for SIMS, clear enhancement of x was detected in both films #2 and #3. The maximum x in each sample was ~0.35 for #3 (averaged $x = 0.19$ along the film thickness area) and ~0.12 for #2 (averaged $x = 0.08$) around the film surface (see the inset of Fig. 4d). This result validates that topotactic chemical reaction occurs as we expected. For sample #2, the hydrogen concentration is much lower than that of #3, indicating that H thermal diffusion was clearly slowed down by the use of a YSZ protection cap. Additionally, an inhomogeneous x distribution along the film-thickness direction is also observed, most strongly for #3. Although a hydrogen diffusion gradient is observed, hydrogen diffused entirely from the surface to film/substrate interface. Figure 5 shows relationship between x determined and lattice parameters. Similar with bulks of H-doped Sm1111 [11], both a - and c -axes lattice parameters of H-doped Sm1111 epitaxial thin films (#2, #3) decreased with increase in x ,

suggesting that the incorporated H continuously replaced with O and electron doping should occur.

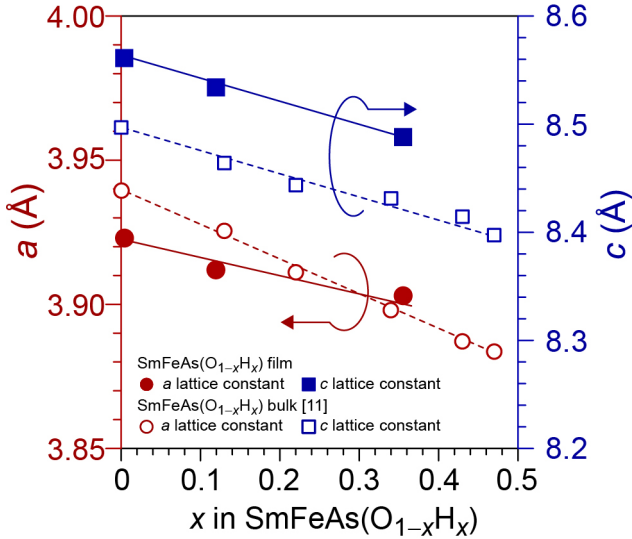


Figure 5. Relationship between x and lattice parameters. Filled red circles and blue squares denote a - and c -axes lattice parameters of fabricated H-doped Sm1111 epitaxial films, where H contents around film surface were employed as x . Open red circles and blue squares correspond to those of H-doped Sm1111 polycrystalline bulks [11].

Superconducting properties

Next, we measured the electronic transport properties of samples #1 – #3. Figures 6a and 6b show $\rho-T$ curves in temperature ranging between 2–300K and 35–54K, respectively. The undoped Sm1111 epitaxial precursor film (#1) exhibited insulator-like behavior, which has been also observed in other 1111-type epitaxial thin films [19, 20, 29 – 31], in contrast to a metallic resistivity in undoped Sm1111 bulks [11]. According to its undoped characteristics, ρ anomaly, which is probably due to an antiferromagnetic transition similar to bulk [11], was observed as indicated by the vertical arrow (T_N). In the H-doped films (#2, #3) a clear metallic resistivity was observed. $\rho-T$ in the T region

higher than 50 K. We performed a power-law fitting for the normal states using an equation $\rho = \alpha + \beta T^n$, where α and β are constants. The exponent n values of normal state were 1.1 for #2 and 0.6 for #3, which are roughly consistent with those of bulks (1.15 at $x = 0.13$ and 0.88 at $x = 0.34$) [11].

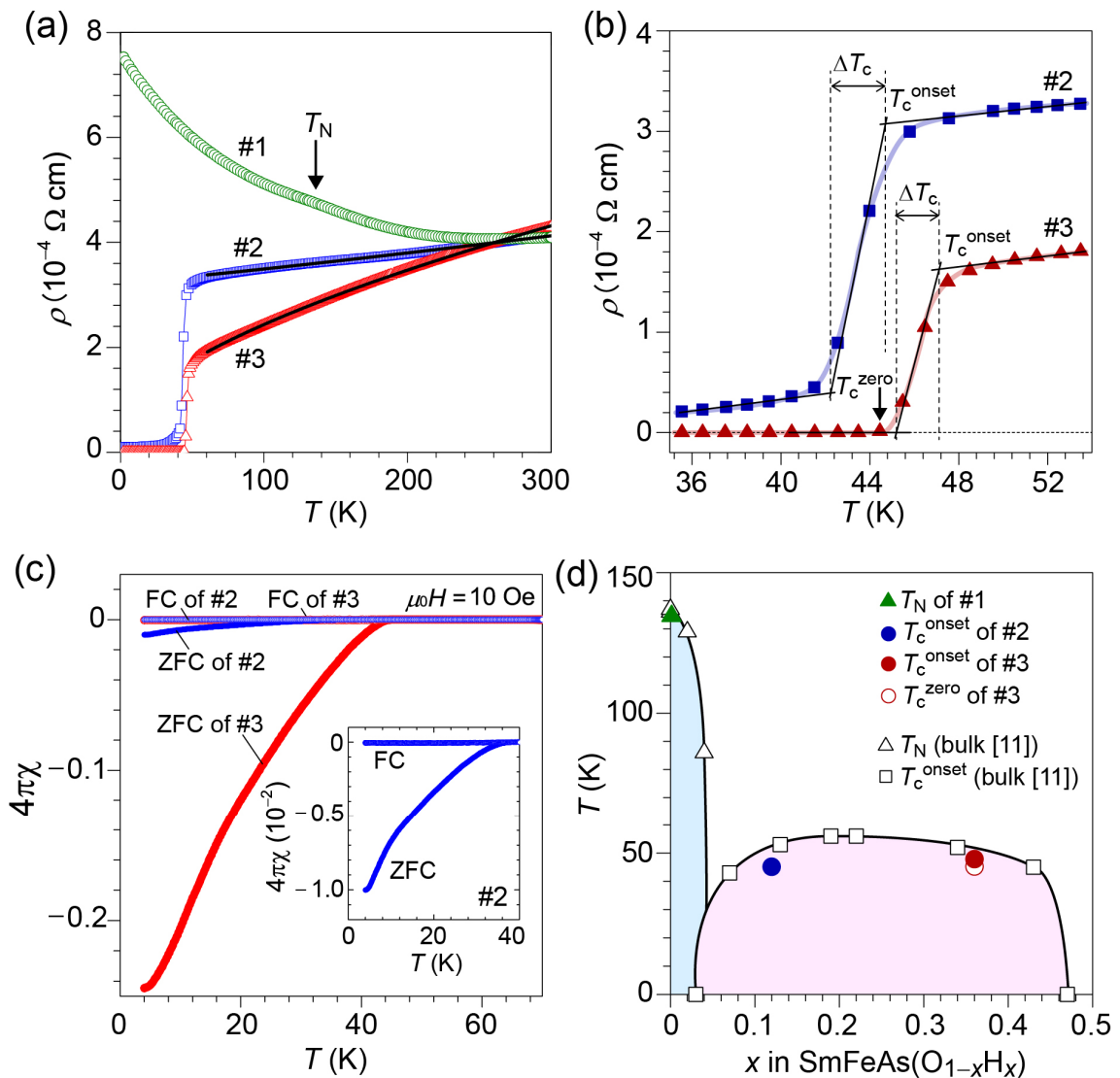


Figure 6. Superconductivity of epitaxial H-doped Sm1111 thin films. (a) Temperature (T) dependence of electrical resistivity (ρ) of #1, #2, and #3 from 2 to 300 K. Néel

temperature (T_N) for #1 is the ρ anomaly temperature due to antiferromagnetic transition. Black lines for #2 and #3 represent fitting results using a power-law equation, $\rho = \alpha + \beta T^n$, where α and β are constants. (b) An enlarged plot of (a) around T_c . T_c^{onset} and T_c^{zero} were defined as T intersection of two fitted linear lines as shown in (b). The transition width ΔT_c is defined as difference between T_c^{onset} and T_c^{zero} . (c) T dependence of the magnetization of #2 and #3 through ZFC and FC measurements under an applied magnetic field of 10 Oe. The inset shows an enlarged view for #2. T_c^{mag} was defined as T where $4\pi\chi$ of ZFC starts to drop from that of FC. (d) The electronic phase diagram of H-doped Sm1111 as a function of x . Open squares and triangles represent T_c and T_N of H-doped Sm1111 bulks that are reported in ref [11]. The filled triangle indicates T_N of #1. Filled circles denote T_c^{onset} of H-doped Sm-1111 epitaxial thin films, with x taken as the maximum H content observed near the film surface.

In the T region lower than 50 K, sharp drops of ρ at 45.2 K for #2 and 47.9 K for #3 indicated a superconducting transition. Although zero resistance was not detected down to 2 K in #2 owing to inhomogeneous and low H concentration, #3 exhibited clear zero resistance at 44.5 K. To confirm its bulk superconductivity state, we measured magnetization as a function of T . Figure 6c shows results of FC and ZFC curves of #2 (blue) and #3 (red). From these results, we concluded that these sharp transitions in $\rho-T$ curves originate from a bulk superconducting state rather than surface superconductivity. This result is the first demonstration of superconductivity in Sm1111 epitaxial thin films by hydrogen doping. The critical temperature T_c determined from electronic and magnetic measurements is summarized in Fig. 6d and Table 1. The T_c^{onset} of our films fit

well to the dome-shaped superconducting phase obtained from polycrystalline bulks, even though the absolute values of T_c were slightly lower compared to the bulk samples probably due to the influence of strain introduced via thin-film growth process. The shielding volume fraction (SVF) was small for #2 (1 %), whereas that of #3 (24.5 %) was enough to judge its bulk superconductivity although it was smaller compared with polycrystalline bulks (79 % for $x = 0.13$ and 77 % for $x = 0.34$) [11]. This relatively small SVF could be attributed to the inhomogeneous H concentration along the film thickness as observed by SIMS (Fig. 4c).

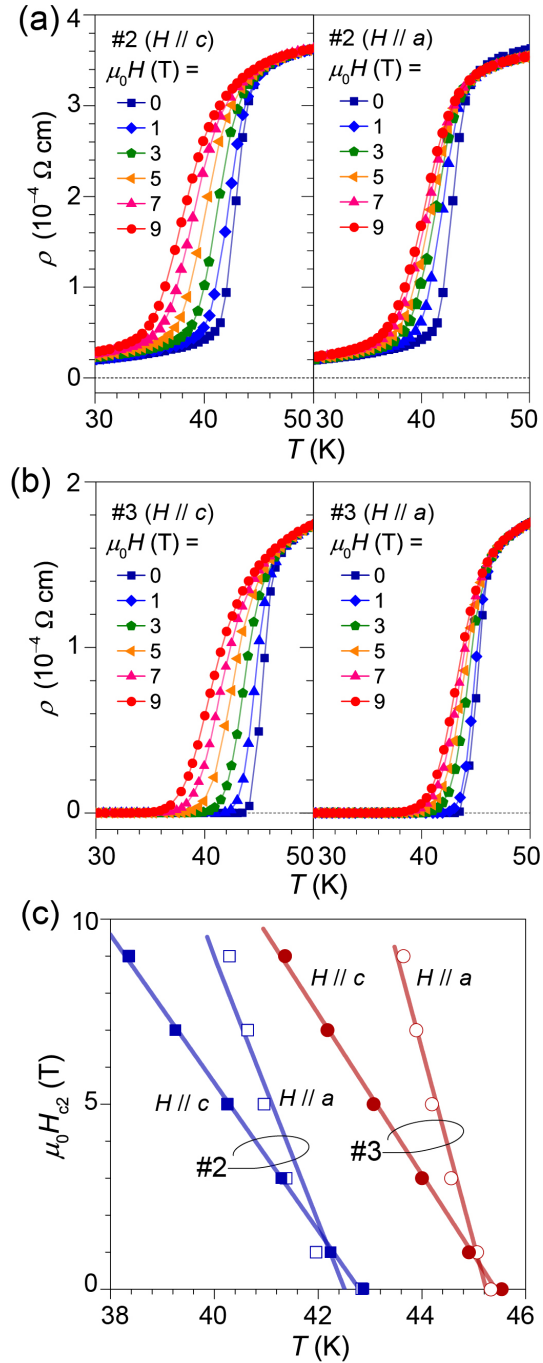


Figure 7. $\rho-T$ curves under magnetic field ($\mu_0 H$) up to 9 T. (a) and (b) are results for #2 and #3, respectively. The applied magnetic fields were along c -axis for left panels and along a -axis for right panels. (d) Relationship between applied $\mu_0 H$ and T_c^{50} , which is defined as temperature where ρ becomes 50 % of the resistivity of the normal state above T_c .

Table 1. Summary of superconducting properties of H-doped Sm-1111 epitaxial films. Anisotropy factor γ is $\gamma = (m_c / m_{ab})^{1/2} = \xi_{ab} / \xi_c = H_{c2}^{\parallel ab} / H_{c2}^{\parallel c}$, where m and ξ are effective mass and coherent length, respectively.

	T_c^{onset} (K)	T_c^{zero} (K)	ΔT_c (K)	T_c^{mag} (K)	SVF (%)	n
#2	45.2	—	3.4	37.1	1.0	1.1
#3	47.9	44.5	3.0	45.0	24.5	0.6
	$H_{c2(0)}^{\parallel c}$ (T)	$H_{c2(0)}^{\parallel a}$ (T)	γ	$\xi^{\parallel c}$ (nm)	$\xi^{\parallel a}$ (nm)	
#2	59	106	1.8	2.4	1.8	
#3	71	172	2.4	2.2	1.4	

Finally, we investigated the superconducting properties of the H-doped Sm1111 films (#2, #3) under magnetic fields. Figures 7a,b shows $\rho-T$ curves of #2, #3 under external magnetic fields at $\mu_0H = 0\text{--}9$ T applied along the c - and a -axes of the epitaxial films, respectively. The superconductivity in #2 and #3 maintained under 9 T both for in-plane and out-of-plane. A rough estimation of the orbital upper critical field, $\mu_0H_{c2}(0)$, from Fig 7c based on the Werthamer–Helfand–Hohenberg theory [32] indicates 172 T and 71 T along a - and c -axes, respectively. The corresponding coherence lengths in the ab

plane ($\xi^{/a}$) and along the c -axis ($\xi^{/c}$) would be 1.4 and 2.2 nm, respectively. For a more realistic description of the upper critical field high magnetic field data beyond 9T is necessary. The anisotropy factor (γ) estimated from $H_{c2}^{/a}$ and $H_{c2}^{/c}$ near T_c was 2.4 for #3, which is comparable with that obtained in F-doped Sm1111 epitaxial films [23] but larger than 1.4 for 122-type K-doped BaFe₂As₂ [33]), owing to insulating SmO blocking layers rather than Ba lattices between the Fe₂As₂ layers.

Summary and outlook

We demonstrated the high- T_c superconductivity up to 48 K of H-doped 1111-type SmFeAsO epitaxial films on MgO single-crystalline substrates, which were grown by a topotactic chemical reaction between undoped epitaxial SmFeAsO precursor films deposited by Nd:YAG PLD and CaH₂ polycrystalline powders using post-deposition thermal annealing. The completely disordered H-doping at O sites was experimentally validated by ABF-STEM microstructure observation. The maximum H concentration with respect to O was ~35 %. This technique is very easy and thus will become an effective and general method to fabricate various high-quality oxyhydride epitaxial films. The relationship between the onset T_c and the maximum H concentration in the films was consistent with the previously established electronic phase diagram of H-doped SmFeAsO polycrystalline samples. We also validated that the observed superconductivity originates from the bulk state in the films, rather than a surface state, by magnetization measurements. The successful fabrication of H-doped Sm1111 films enables future investigations of their electronic structure by angle-resolved photoemission spectroscopy in order to elucidate the still controversially debated mechanism of superconductivity in Fe-based superconductors. Currently investigations

of the critical current densities, which are an important property for applications such as high-field magnets, are carried out in the high- T_c 1111-type epitaxial films.

Acknowledgments

This work was supported by the Ministry of Education, Culture, Sports, Science, and Technology (MEXT) through the Element Strategy Initiative to Form Core Research Center. The authors thank Dr. Soshi Iimura for providing us a standard polycrystalline bulk sample, SmFeAs(O_{0.4}H_{0.6}), to perform quantitative chemical composition analysis by SIMS. T. K. was also supported by PRESTO, Japan Science and Technology Agency (Grant No. JPMJPR16R1). H. Hi. was also supported by the Japan Society for the Promotion of Science (JSPS) through Grants-in-Aid for Scientific Research (A) and (B) (Grant Nos. 17H01318 and 18H01700), and Support for Tokyotech Advanced Research (STAR).

Competing interests

The authors declare no competing interests.

Author contributions

J. M., K. H., S. H., and T. K. performed thin-film growth and related experiments. M. S. observed STEM images. H. Hi. and H. Ho. supervised this study. All the authors contributed to discussion and writing the draft.

Supplementary Information

Supplementary Figures S1 and S2 are XRD patterns of in-situ Nd:YAG PLD grown films and their $\rho-T$ curves, respectively.

References

1. Kamihara, Y., Watanabe, T., Hirano, M., Hosono, H. Iron-Based Layered Superconductor La[O_{1-x}F_x]FeAs ($x = 0.05\text{--}0.12$) with $T_c = 26$ K. *J. Am. Chem. Soc.* **130**, 3296–3297 (2008).
2. Kamihara, Y., Hiramatsu, H., Hirano, M., Kawamura, R., Yanagi, H., Kamiya, T., Hosono, H. Iron-Based Layered Superconductor: LaOFeP. *J. Am. Chem. Soc.* **128**, 10012–10013 (2006).

3. For a review, Hiramatsu, H., Kamioka, H., Ueda, K., Ohta, H., Kamiya, T., Hirano, M., Hosono, H. Opto-electronic properties and light-emitting device application of widegap layered oxychalcogenides: LaCuOCh (Ch = chalcogen) and $\text{La}_2\text{CdO}_2\text{Se}_2$. *phys. stat. sol. (a)* **203**, 2800–2811 (2006).
4. Hiramatsu, H., Kamiya, T., Tohei, T., Ikenaga, E., Mizoguchi, T., Ikuhara, Y., Kobayashi, K., Hosono, H. Origins of Hole Doping and Relevant Optoelectronic Properties of Wide Gap p-Type Semiconductor, LaCuOSe . *J. Am. Chem. Soc.* **132**, 15060–15067 (2010).
5. For a review, Hosono, H., Tanabe, K., Takayama-Muromachi, E., Kageyama, H., Yamanaka, S., Kumakura, H., Nohara, M., Hiramatsu, H., Fujitsu, S. Exploration of new superconductors and functional materials, and fabrication of superconducting tapes and wires of iron pnictides. *Sci. Technol. Adv. Mater.* **16**, 033503 (2015).
6. For a review, Putti, M. *et al.* New Fe-based superconductors: properties relevant for applications. *Supercond. Sci. Technol.* **23**, 034003 (2010).
7. For a review, Shimoyama, J. Potentials of iron-based superconductors for practical future materials. *Supercond. Sci. Technol.* **27**, 044002 (2014).
8. For a review, Hosono, H., Yamamoto, A., Hiramatsu, H., Ma, Y. Recent advances in iron-based superconductors toward applications. *Mater. Today* **21**, 278–302 (2018).
9. For a review, Iida, K., Hänsch, J., Tarantini, C. Fe-based superconducting thin films on metallic substrates: Growth, characteristics, and relevant properties. *Appl. Phys. Rev.* **5**, 031304 (2018).
10. Ren, Z.-A., Lu, W., Yang, J., Yi, W., Shen, X.-L., Li, Z.-C., Che, G.-C., Dong, X.-L., Sun, L.-L., Zhou, F., Zhao, Z.-X. Superconductivity at 55K in Iron-Based F-Doped Layered Quaternary Compound $\text{Sm}[\text{O}_{1-x}\text{F}_x]\text{FeAs}$. *Chin. Phys. Lett.* **25**, 2215–2216 (2008).
11. Hanna, T., Muraba, Y., Matsuishi, S., Igawa, N., Kodama, K., Shamoto, S., Hosono, H. Hydrogen in layered iron arsenides: Indirect electron doping to induce superconductivity. *Phys. Rev. B* **84**, 024521 (2011).
12. Iimura, S., Matsuishi, S., Sato, H., Hanna, T., Muraba, Y., Kim, S. W., Kim, J. E., Takata, M., Hosono, H. Two-dome structure in electron-doped iron arsenide superconductors. *Nat. Commun.* **3**, 943 (2012).
13. Iimura, S., Okanishi, H., Matsuishi, S., Hiraka, H., Honda, T., Ikeda, K., Hansen, T. C., Otomo, T., Hosono, H. Large-moment antiferromagnetic order in overdoped high- T_c superconductor $^{154}\text{SmFeAsO}_{1-x}\text{D}_x$. *Proc. Natl. Acad. Sci. USA* **114**, E4354–E4359 (2017).
14. Iimura, S., Muramoto, T., Fujitsu, S., Matsuishi, S., Hosono, H. High pressure

- growth and electron transport properties of superconducting $\text{SmFeAsO}_{1-x}\text{H}_x$ single crystals. *J. Asian Ceram. Soc.* **5**, 357–363 (2017).
15. For a review, Hiramatsu, H., Katase, T., Kamiya, T., Hosono, H. Thin Film Growth and Device Fabrication of Iron-Based Superconductors. *J. Phys. Soc. Jpn.* **81**, 011011 (2012).
 16. For a review, Haindl, S., Kidszun, M., Oswald, S., Hess, C., Büchner, B., Kölling, S., Wilde, L., Thersleff, T., Yurchenko, V. V., Jourdan, M., Hiramatsu, H., Hosono, H. Thin film growth of Fe-based superconductors: from fundamental properties to functional devices. A comparative review. *Rep. Prog. Phys.* **77**, 046502 (2014).
 17. Backen, E., Haindl, S., Niemeier, T., Hühne, R., Freudenberg, T., Werner, J., Behr, G., Schultz, L., Holzapfel, B. Growth and anisotropy of $\text{La}(\text{O}, \text{F})\text{FeAs}$ thin films deposited by pulsed laser deposition. *Supercond. Sci. Technol.* **21**, 122001 (2008).
 18. Haindl, S., Kidszun, M., Kauffmann, A., Nenkov, K., Kozlova, N., Freudenberger, J., Thersleff, T., Hänsch, J., Werner, J., Reich, E., Schultz, L., Holzapfel, B. High Upper Critical Fields and Evidence of Weak-Link Behavior in Superconducting $\text{LaFeAsO}_{1-x}\text{F}_x$ Thin Films. *Phys. Rev. Lett.* **104**, 077001 (2010).
 19. Hiramatsu, H., Katase, T., Kamiya, T., Hirano, M., Hosono, H. Heteroepitaxial growth and optoelectronic properties of layered iron oxyarsenide, LaFeAsO . *Appl. Phys. Lett.* **93**, 162504 (2008).
 20. Haindl, S., Hanzawa, K., Sato, H., Hiramatsu, H., Hosono, H. *In-situ* growth of superconducting $\text{SmO}_{1-x}\text{F}_x\text{FeAs}$ thin films by pulsed laser deposition. *Sci. Rep.* **6**, 35797 (2016).
 21. Haindl, S., Molatta, S., Hiramatsu, H., Hosono, H. Recent progress in pulsed laser deposition of iron based superconductors. *J. Phys. D.: Appl. Phys.* **49**, 345301 (2016).
 22. Haindl, S., Kinjo, H., Hanzawa, K., Hiramatsu, H., Hosono, H. Pulsed laser deposition of $\text{SmFeAsO}_{1-\delta}$ on $\text{MgO}(100)$ substrates. *Appl. Surf. Sci.* **437**, 418–428 (2018).
 23. Haindl, S., Kampert, E., Sasase, M., Hiramatsu, H., Hosono, H. Low anisotropic upper critical fields in $\text{SmO}_{1-x}\text{F}_x\text{FeAs}$ thin films with a layered hybrid structure. *Supercond. Sci. Technol.* **32**, 044003 (2019).
 24. Kawaguchi, T., Uemura, H., Ohno, T., Tabuchi, M., Ujihara, T., Takenaka, K., Takeda, Y., Ikuta, H. In situ growth of superconducting NdFeAs(O,F) thin films by molecular beam epitaxy. *Appl. Phys. Lett.* **97**, 042509 (2010).
 25. For a review, Sakoda, M., Iida, K., Naito, M. Recent progress in thin-film growth of Fe-based superconductors: superior superconductivity achieved by thin films.

Supercond. Sci. Technol. **31**, 093001 (2018).

26. Corrales-Mendoza, I., Labias-Romero, J., Castillo, N., Conde-Gallardo, A. Growth of $\text{SmFeAsO}_{1-x}\text{F}_x$ and $\text{NdFe}_{1-x}\text{Co}_x\text{AsO}$ thin films by metal-organic chemical vapor deposition and post diffusion processes. *Supercond. Sci. Technol.* (accepted manuscript, DOI: 10.1088/1361-6668/ab098f).
27. Hiramatsu, H., Matsuda, S., Sato, H., Kamiya, T., Hosono, H. Growth of *c*-Axis-Oriented Superconducting KFe_2As_2 Thin Films. *ACS Appl. Mater. Interfaces* **6**, 14293–14301 (2014).
28. Hatakeyama, T., Sato, H., Hiramatsu, H., Kamiya, T., Hosono, H. Novel solid-phase epitaxy for multi-component materials with extremely high vapor pressure elements: An application to KFe_2As_2 . *Appl. Phys. Express* **9**, 055505 (2016).
29. Kawaguchi, T., Uemura, H., Ohno, T., Watanabe, R., Tabuchi, M., Ujihara, T., Takenaka, K., Takeda, Y., Ikuta, H. Epitaxial Growth of NdFeAsO Thin Films by Molecular Beam Epitaxy. *Appl. Phys. Express* **2**, 093002 (2009).
30. Ueda, S., Takeda, S., Takano, S., Mitsuda, A., Naito, M. Molecular Beam Epitaxy Growth of Superconducting $\text{Ba}_{1-x}\text{K}_x\text{Fe}_2\text{As}_2$ and SmFeAs(O,F) Films. *Jpn. J. Appl. Phys.* **51**, 010103 (2012).
31. Takeda, S., Ueda, S., Takano, S., Yamamoto, A., Naito, M. Growth of superconducting SmFeAs(O, F) epitaxial films by F diffusion. *Supercond. Sci. Technol.* **25**, 035007 (2012).
32. Helfand, E., Werthamer, N. R. Temperature and Purity Dependence of the Superconducting Critical Field, H_{c2} . II. *Phys. Rev.* **147**, 288 – 294 (1966).
33. Yuan, H. Q., Singleton, J., Balakirev, F. F., Baily, S. A., Chen, G. F., Luo, J. L., Wang, N. L. Nearly isotropic superconductivity in $(\text{Ba},\text{K})\text{Fe}_2\text{As}_2$. *Nature* **457**, 565–568 (2009).

Supplementary Information for “Superconductivity at 48 K of heavily hydrogen-doped SmFeAsO epitaxial films grown by topotactic chemical reaction using CaH₂”

Jumpei Matsumoto (1), Kota Hanzawa (1), Masato Sasase (2), Silvia Haindl (3),
Takayoshi Katase (1), Hidenori Hiramatsu (1,2,a), and Hideo Hosono (1,2)

(1) Laboratory for Materials and Structures, Institute of Innovative Research, Tokyo Institute of Technology, Mailbox R3-3, 4259 Nagatsuta-cho, Midori-ku, Yokohama, Kanagawa 226-8503, Japan

(2) Materials Research Center for Element Strategy, Tokyo Institute of Technology, Mailbox SE-1, 4259 Nagatsuta-cho, Midori-ku, Yokohama, Kanagawa 226-8503, Japan

(3) World Research Hub Initiative (WRHI), Institute of Innovative Research, Tokyo Institute of Technology, 4259 Nagatsuta-cho, Midori-ku, Yokohama, Kanagawa 226-8503, Japan

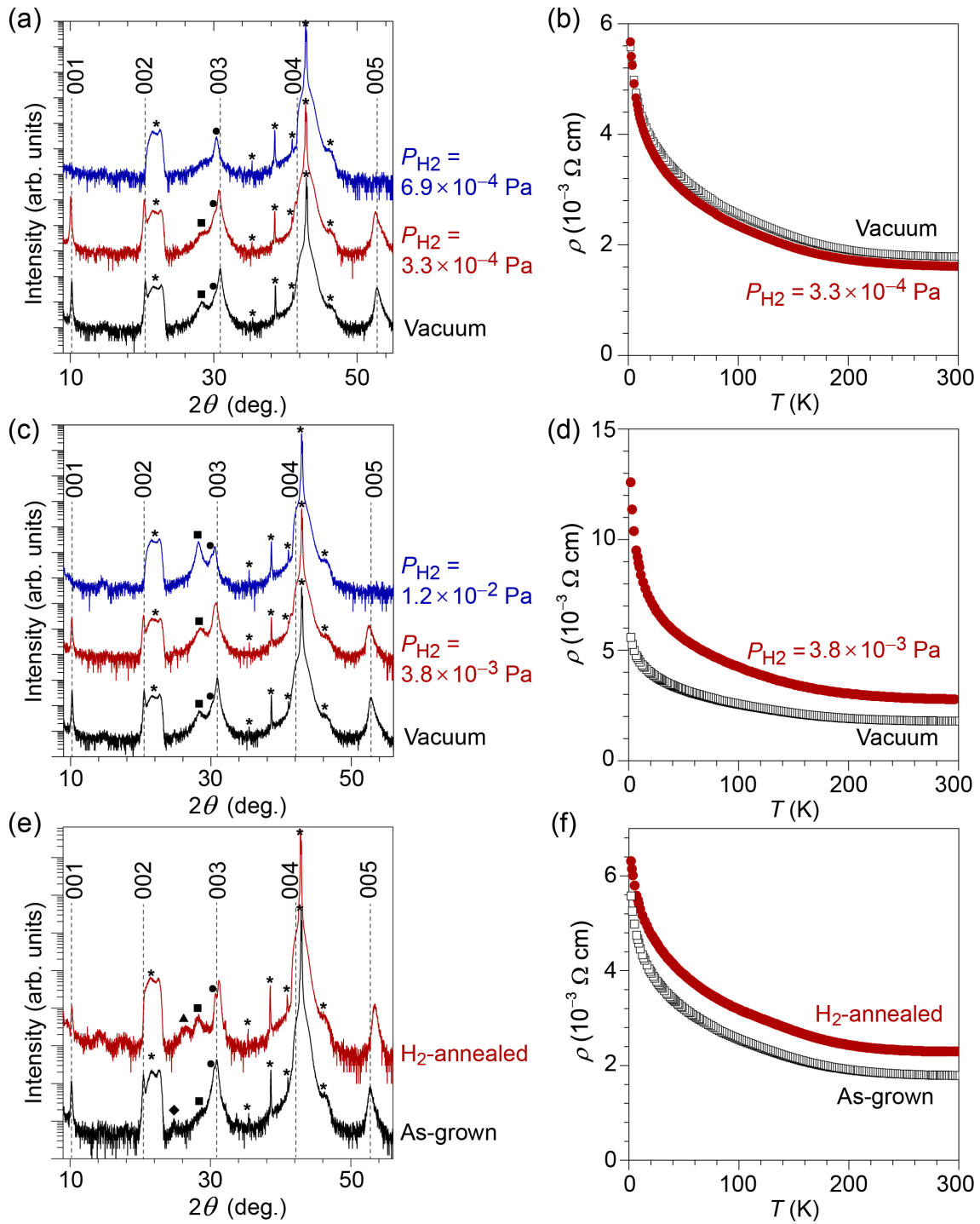


Figure S1. Summary of preliminary experimental H-doping attempts for Sm1111 epitaxial films. (a) XRD patterns for the as-grown Sm1111 film deposited under high vacuum by Nd:YAG PLD (black curve) and films deposited under different partial hydrogen gas pressure (P_{H_2}) (red and blue curves). (b) Temperature (T) dependence of electrical resistivity (ρ) of the obtained films in (a). (c) XRD patterns of Sm1111 films grown by Nd:YAG PLD at different P_H , where H radical gas was introduced through an

rf-plasma generator operating at 150 W. (d) ρ - T curves as a function of P_{H_2} for (c). (e) Effect of post-deposition thermal annealing under H_2 atmosphere for as-grown Sm1111 epitaxial films. The internal H_2 gas pressure in the furnace was maintained to be 1 – 2 MPa. (f) ρ - T curves for as-grown and H-annealed Sm1111 in (e). In (a), (c), and (e), dotted lines, asterisks, circles, squares, diamond, and triangle represent diffraction peak positions originating from Sm1111 00 l , MgO substrate, SmAs 200, a possible impurity phase of Sm_2O_3 222 or $\text{Sm}_3\text{Fe}_5\text{O}_{12}$ 400, SmAsO₄ 200, and $\text{Sm}_3\text{Fe}_5\text{O}_{12}$ 321, respectively.

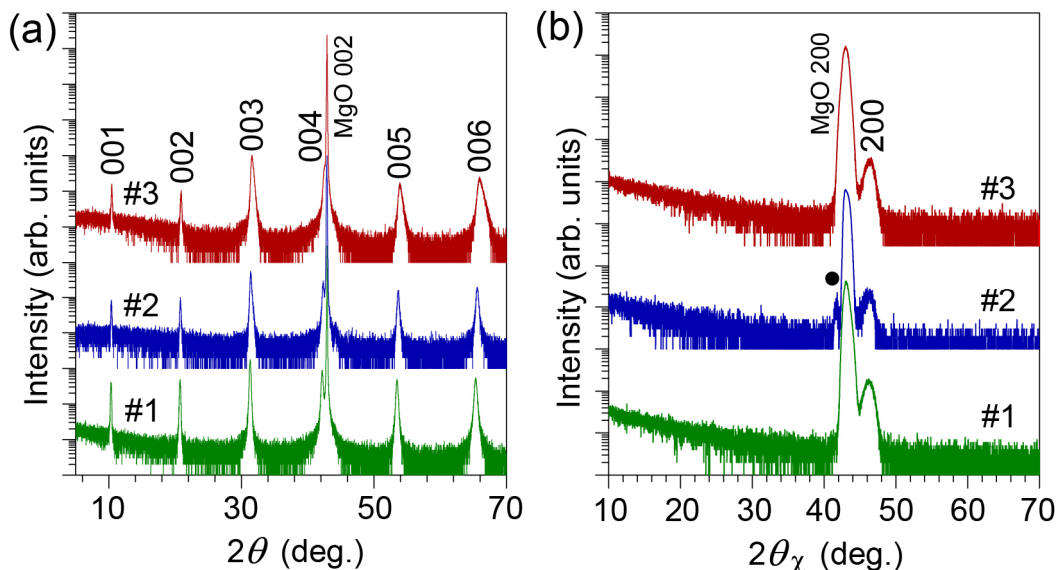


Figure S2. Wide-angle range XRD patterns of Figs. 2a for (a) out-of-plane and 2b for (b) in-plane. Filled circle indicates a diffraction attributed to an impurity phase, possibly As_2O_5 .